Performance Prediction and Multipath Interference Mitigation for a Downlooking Synthetic Aperture Sonar

Shannon-Morgan Steele
Kraken Robotic Systems Inc.
Dartmouth, NS, Canada
ssteele@krakenrobotics.com

Richard Charron
Kraken Robotic Systems Inc.
Mount Pearl, NL, Canada
rcharron@krakenrobotics.com

Jeremy Dillon
Kraken Robotic Systems Inc.
Dartmouth, NS, Canada
jdillon@krakenrobotics.com

***Abstract*—Sub-bottom seabed imaging is a valuable tool for a variety of applications including mine hunting, cable route planning, geological exploration, and wind farm installation. The typical high frequency Synthetic Aperture Sonars (SAS) used for seabed imaging are subject to rapid attenuation in the sub-bottom, and thus, low-frequency (less than 100 kHz) sonars must be used for sub-bottom imaging. Operating the SAS in a downlooking orientation trades area coverage rate for better imaging depth capability; however, the performance can become limited by multipath interference between the vehicle and the seafloor. In this paper, we propose a new method for suppressing multipath using the pulse repetition period. To demonstrate the performance gain of our proposed multipath suppression method, we have developed a new model for the downward looking SAS configuration. The predicted performance of the downward looking SAS is optimized in a variety of mission scenarios. Performance metrics analyzed include maximum depth for buried target detection, resolution, across-track performance envelope, and area coverage rate. It is shown that a judicious choice of the pulse repetition period can eliminate multipath interference by causing spurious echoes to arrive outside of the imaging region of interest.**

***Index Terms*—synthetic aperture, sonar, sub-bottom imaging, downlooking, multipath**

I. Introduction

Synthetic Aperture Sonar (SAS) is a high-resolution acoustic imaging tool that exploits the along-track motion of the sensor platform to synthesize an image with resolution that is both range and frequency independent. High frequency SAS can generate centimetric resolution images of the seafloor and surface targets; however, these systems cannot detect buried objects due to rapid acoustic attenuation in sediment. Low Frequency Synthetic Aperture Sonar (LFSAS) signals can propagate into the seabed and image targets at a much higher resolution in comparison to sub-bottom profilers. Typically, SAS is operated in a side-looking configuration to maximize the Area Coverage Rate (ACR). The low grazing angles of a side-looking configuration severely limit the burial depth to which an object can be detected, largely due to the critical grazing angle [1], [2]. In a downward looking configuration, LFSAS has the potential to detect objects to much greater depths.

LFSAS has several advantages over high frequency SAS systems. Lower attenuation in both the water column and sediment allows LFSAS to image and detect objects at greater burial depths and range. High frequency acoustics can only present the geometric shape of objects on the seafloor, making it difficult to discriminate between targets in cluttered environments. LFSAS has the potential to reduce false alarm rates and discriminate between man-made objects and seabed clutter by operating in the structural acoustics regime (1–50 kHz). In the structural acoustic regime, resonant (elastic) modes of the target structures and internal components are excited. These resonant modes can aid the detection and classification of targets of specific interest.

Designing and operating a low-frequency sonar presents a variety of challenges in terms of optimizing and predicting sonar performance, especially in strong multipath (MP) scenarios. It is ideal to fly the vehicle at low altitudes to maximize depth and resolution performance. However, these performance gains come at the expense of reduced ACR and increased MP, as it is expected that interference caused by sound reflecting between the seabed and the vehicle will be the limiting factor for large vehicles operating at low altitudes.

We have formulated a model using the active sonar equation to evaluate downlooking SAS performance. Sonar performance prediction modeling using the sonar equation has been well studied for a variety of different cases; however, the performance prediction for a downlooking low-frequency SAS has not been well demonstrated, especially for the purpose of detecting objects buried below the seafloor. In addition to the standard components of the sonar equation (source level, directivity index, transmission loss, target strength, and noise level), the model also incorporates performance parameters specific to SAS and downlooking sub-bottom imaging systems including SAS processing gain, frequency dependent sediment attenuation, depth dependent range resolution, and beamwidth and bandwidth limited ensonified volume. The noise interference component of the model includes a rigorous treatment of MP along with ambient and self (electronic) noise. The MP model captures the impact of numerous reflections between the vehicle and the seafloor whose time evolution is on a much

larger scale than the direct return of interest. Also included in the MP model are terms accounting for key environmental and operational parameters such as sediment type, vehicle size, and Pulse Repetition Period (PRP).

In this paper, we illustrate performance prediction results for the LF band of Kraken's AquaPix® Multispectral SAS [1] in a downlooking configuration. The downlooking LFSAS is an acoustic sensor operating in the frequency range of 15-30 kHz, consisting of a single flat-faced transmitter and a planar receive array, allowing for beamforming in the along and across track directions. The downlooking LFSAS receiver has a modular embodiment, to form longer receiver apertures across-track and thus achieve higher ACR and better resolution. The current embodiment of the downlooking LFSAS is designed to fit on the Kraken ThunderFish® XL Autonomous Underwater Vehicle (AUV), which is currently under development as a hover-capable AUV for subsea resident applications. LFSAS performance predictions in various mission scenarios are presented. Mission scenarios include buried target detection while operating in an environment supporting a variety of MP interference mechanisms.

II. Performance Prediction Model

A. Resolution

Sidelooking SAS geometry is generally defined by two directions, the along track and across track direction, which we denote as x and y. For downlooking SAS, we must also introduce a third direction, the depth direction, z. Typically, SAS systems use a matched filtered broadband frequency modulated chirp to achieve high range resolution. For the sidelooking case, this range resolution would correspond to the y direction; however, for downlooking SAS, the range resolution corresponds to the z direction. The resolution in the z direction of the downlooking SAS (δ_z) is defined as

$$\delta_z = \frac{C}{2B}, \tag{1}$$

where B is the bandwidth of the transmitted pulse and C is the speed of sound in the medium the sound is propagating in [3]. In the water column and while imaging the seabed surface, C is the speed of sound in the water column. For sub-bottom imaging, C is the speed of sound in the sediment.

SAS processing is applied in the along track direction, and thus the resolution can be expressed in terms of the length of the sonar pulse center wavelength (λ), synthetic aperture length (L_{SAS}), and the slant range to the seabed (r)

$$\delta_x = \frac{r\lambda}{2L_{SAS}}, \tag{2}$$

which is equivalent to half the along track length of the transmitter [3].

In the across track direction, the downlooking LFSAS geometry is similar to a mutli-beam echosounder, where we steer the mutli-element array to various elevation angles, θ, across the swath. The across track resolution (δ_y) is thus determined by the sonar footprint in the across track direction

$$\delta_y = h \sec^2 \theta \sin \phi, \tag{3}$$

where h is the altitude above the seabed, and ϕ is the across track beamwidth [4]. The elevation angle is dependent on the slant range to the seabed, and thus the resolution decreases as the elevation angle grows.

Beampattern simulations indicate the downlooking LFSAS can achieve approximately 20 cm across track resolution from an altitude of 5 m. At 5 m altitude the across track resolution varies only slightly with the across track distance from the sonar (Figure 1).

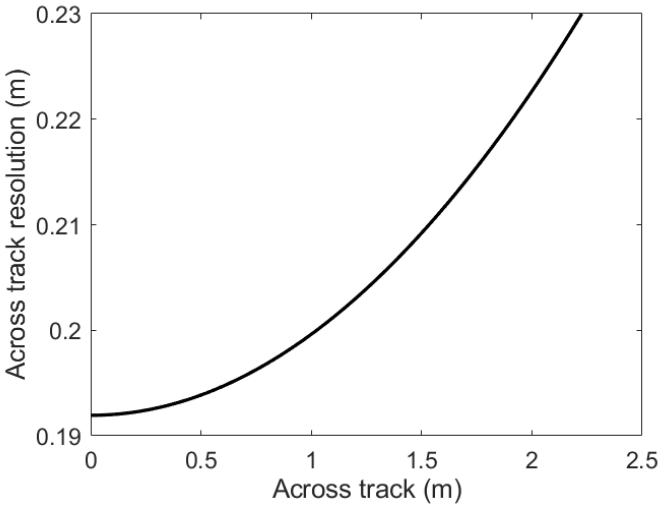

Fig. 1. Across track resolution as a function of across track distance.

Through SAS processing, the downlooking LFSAS can achieve a resolution of 15 cm in the along track direction. In the depth direction, the effect of sediment attenuation degrades the high frequency components of a linear frequency-modulated (LFM) pulse at a faster rate than the low frequency components. As a result, cross-correlation of the received signal with the source pulse results in a broadening of the main lobe, increased sidelobe levels, and an asymmetry in the sidelobe structure of the compressed signal, all of which lead to a progressive resolution loss and reduced signal-to-total-reverberation ratio as a function of depth below seafloor. Figure 2 illustrates the estimated resolution for medium sand and silt seabeds as a function of depth below the seafloor to 2 m depth, including the effect of a shading function to improve the mainlobe-to-sidelobe level ratio.

B. Signal to Noise Ratio

To make the sonar equation applicable to buried object detection there are additional challenges that must be addressed, which include sediment attenuation and sediment interface transmission. In the downlooking configuration, it is best to operate close to the seabed so that reasonable depth and across track resolution can be realized. Operating a large vehicle at

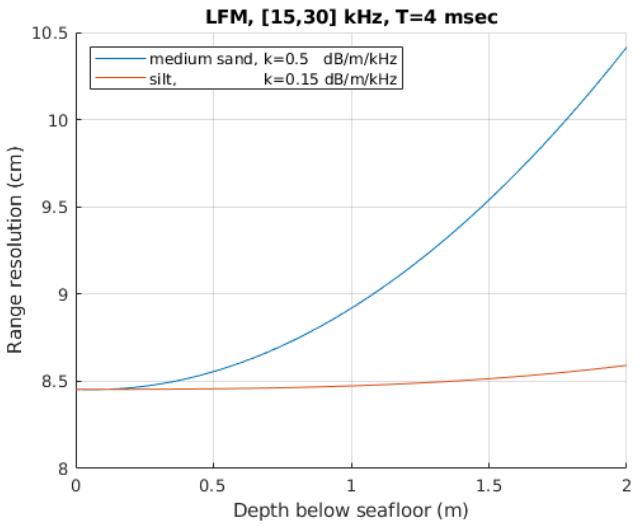

Fig. 2. Depth resolution as a function of depth into the seabed for a 4 millisecond 15–30 kHz LFM transmit pulse. Acoustic attenuation coefficients k are provided in the legend.

low altitude can introduce significant MP interference. All of these factors can be included in a sonar performance model by accounting for them in the appropriate terms of the sonar equation

$$SL - TL + TS - NL + DI > DT \tag{4}$$

where SL is the source level, TL is transmission loss, TS is target strength, NL is noise level, DI is the directivity index, and DT represents a detection threshold.

The directivity index includes sensitivity in both azimuth directions of a single receiver element, as the calculated SNR on the left hand side of (4) is for an individual element.

In the transmission loss term, we account for spherical spreading and absorption in both the sediment and water column as well as the sediment interface transmission coefficient and subcritical angle seabed penetration. The sediment attenuation is dependent on frequency and sediment type; here, we use the attenuation coefficients provided in the APL-UW handbook [5]. The sediment interface transmission coefficient T is calculated using the continuity of pressure ($T = 1 + R$), where R is the Rayleigh reflection coefficient for a given grazing angle. The transmission angle into the sediment is calculated using Snell's law. If the grazing angle becomes equal to or less than the critical angle all transmitted sound will travel horizontally along the water sediment interface, and thus there will be no acoustic return. Numerous field trials have demonstrated that this behaviour is not observed, and subcritical acoustic returns are possible [2]. Not accounting for such anomalous scattering may cause us to under predict the downlooking LFSAS performance. Thus, we have included a small-roughness perturbation model of subcritical penetration.

High-frequency (greater than 5 kHz) subcritical penetration in the seabed can be caused by either refraction of a Slow Wave or scattering by sediment roughness and volume heterogeneity [2]. Due to stronger evidence of sediment scattering being the true mechanism [6]–[8], this model only considers subcritical penetration due to sediment roughness scattering. For the performance prediction model, we used the roughness perturbation methods described in [7], [9].

Through the noise level term we account for ambient noise, self (electronic) noise, multipath interference, and, in the case of target detection, seabed backscatter response. The ambient noise level is estimated based on the Wenz curves [10], which is calculated using the sea state as well as the center frequency and bandwidth of the receiver. The APL-UW backscattering model was used to simulate the seabed backscatter response [5]. The model includes contributions from the sediment interface roughness and volume scattering. The ensonified region of the backscattered response was determined using the methods described in [11].

It is expected that the greatest contributor to the multipath interference will be the path between the vehicle and the seabed. In this scenario the sound can "bounce" between the vehicle multiple times, producing a beating pattern of interfering echoes whose rate of decay is much slower than the signal propagating along the direct downward path into the seabed. This can create a complicated multipath modeling exercise as we must keep track of the multipath history of several previous transmit cycles in addition to the direct return and multipath of the current ping. Further details on the multipath interference implementation can be found in Appendix A.

For target strength calculations the standard formulas provided by Urick in [12] are generally sufficient. Of particular interest to our application are the expressions for spheres, finite cylinders, and infinite cylinders. A cylinder is considered infinite if its length (l) in terms of wavelength (λ) is greater than the range (r) to the target

$$r < \frac{l^2}{\lambda}. \tag{5}$$

In the target strength term we also account for the pulse compression gain (PG) and the SAS gain (SG). It is important to note that these gains are applied differently depending on whether the target of interest is an object or the seabed. Equation (6) is the PG applied in the case of object detection, where T is the pulse length and B is the bandwidth. In the case of the seabed, the pulse compression gain does not need to be applied because the increased echo level due to pulse compression is exactly offset by a reduction in the resolution cell size from $\frac{CT}{2}$ to $\frac{C}{2B}$.

$$PG = 10\log_{10}(BT) \tag{6}$$

Within this pulse compression gain we account for the attenuating (decreasing) bandwidth as a function of depth into the seabed that one can deduce from the diminishing range resolution calculations discussed earlier.

For spheres, the SAS gain is dependent on the along track resolution, δx, as

$$SG = 10\log_{10}\left(\frac{L_{SAS}}{\delta x}\right), \tag{7}$$

where L_{SAS} is the length of the synthetic aperture. For cylinders, the SAS gain is dependent on the diameter d, length l, and orientation ψ of the cylinder relative to the along track direction

$$SG = 10\log_{10}\left(\min\left\{\frac{L_{SAS}}{\delta x}, \frac{L_{SAS}}{\Psi}\right\}\right) \tag{8}$$

where $\Psi = \max\{d, l\sin(\psi)\}$. The orientation is defined such that ψ is 90° when the cylinder trends in the along track direction, and 0° if it is trending in the across track direction.

C. Simulations

This paper presents simulations of buried target detection performance in a deep water environment (200 m depth). Both medium sand and silt seabeds were simulated, and all seabeds were assumed to be flat (non-sloping). For targets, buried spheres and cylinders were considered, with their target strength being calculated using the target strength equations from [12]. Both finite cylinders, representative of UXO's, and infinite cylinders, representative of a reinforced communication cable or pipeline, were simulated. Maximum burial depths were modeled over a wide range of target diameters. For the finite cylinder, a diameter to length aspect ratio of 0.5 was used, while the infinite cylinders were assigned a length of 10 m. The target detection threshold (signal-to-total-interference ratio) for all simulations was set to 10 dB.

Here, the sonar source level was assumed to be 200 dB and the pulse length 4 ms. The hydrophone sensitivity was measured from a prototype array to be –188 dB re V/μPa. The DI for both the transmitter and an individual element on the receiver were from standard models. All simulations use a sea state of 3, wind speed of 10 knots, 4°C water temperature, 35 ppt salinity, and pH of 8.

III. Multipath mitigation using pulse repetition period

One approach to limiting MP interference with an acoustic signal is to ping slowly, allowing the reverberation to diminish to the level of self or ambient noise between each transmit cycle. This approach severely limits the survey speed (and thus ACR) because the SAS aperture needs to be adequately sampled [13]. Here, we propose an alternative solution, which is to choose an optimal PRP based on the imaging geometry. Typically, we determine the pulse repetition period PRP_0 for adequate sampling in the along track direction based on vehicle speed (υ) and receiver array length (L_a):

$$PRP_0 = \frac{L_a}{2\upsilon} \tag{9}$$

A typical wide-body vehicle speed is 2–3 knots so that the SAS sampling criterion would suggest a ping rate of 10–15 Hz, but our simulations indicate that such a setting will yield a target return embedded in a significant MP interference pattern from a previous ping (Fig. 3, red line). Thus, the sonar is only capable of imaging targets to a short range below the seafloor. There is therefore an opportunity to mitigate the multipath interference by modifying the PRP expression in (Eq. 9) to

$$PRP = \frac{L_a}{2\upsilon} - \tau, \tag{10}$$

where $\tau > 0$, which in effect decreases the pulse repetition period (i.e., pinging more frequently). τ is limited by the desired two-way travel time (χ) needed to cover the range of interest to ensure the sonar achieves full ACR.

$$\tau \leq \frac{L_a}{2\upsilon} - \chi. \tag{11}$$

The mulitpath locations (total travel distance) of the previous ping (η) can be used to determine τ

$$\eta(n) = \frac{PRP_0 C_w}{2} - nr - h, \tag{12}$$

where, C_w is the nominal water column sound speed, r is the slant range to the seabed (equivalent to h unless the transmitter or receiver are tilted), and $n = 1, 2, \ldots$ is an index denoting the number of two-way returns between the vehicle and seafloor (see Appendix A for details). Unlike the multipath interference model presented in Appendix A, we assume here the greatest contributor to the multipath interference is from the previous ping as we don't consider contributions from earlier previous pings. The more general treatment in Appendix A considers multiple previous pings. Once all the locations of the previous ping's multipath history is computed, we select the multipath location $\hat{\eta}$ that is closest in arrival time to the current ping's direct seabed arrival, and τ can then be calculated as

$$\tau = \frac{\chi - h - \hat{\eta}}{C_w} \tag{13}$$

Utilizing (10), we can force the interference to the outer limits of our signal, effectively removing the impact of MP on the current ping's direct return (Fig. 3, blue line) while maintaining ACR. For example, while imaging targets in a medium sand at an altitude of 5m, our PRP MP suppression method increases the target detection depth to the ambient/self noise limit, increasing the maximum target detection depth by 60 cm (Fig. 3).

For this PRP selection method to work consistently, the vehicle needs to maintain constant altitude. The exact altitude sensitivity is dependent on the distance between the noise limited (no MP interference) maximum detection depth and the location of the shifted multipath. For example in the case of Fig. 3, the altitude sensitivity would be about 1.75 m. So as long as the AUV can maintain altitude to that level of accuracy (which is likely, especially in deep water), this method for PRP selection is suitable. It is also important to note that, as long as the altitude isn't varying too rapidly, the PRP could be updated in real time to account for significant altitude changes.

If the vehicle altitude relative to the seafloor is highly variable it may not be practical to continuously re-model the

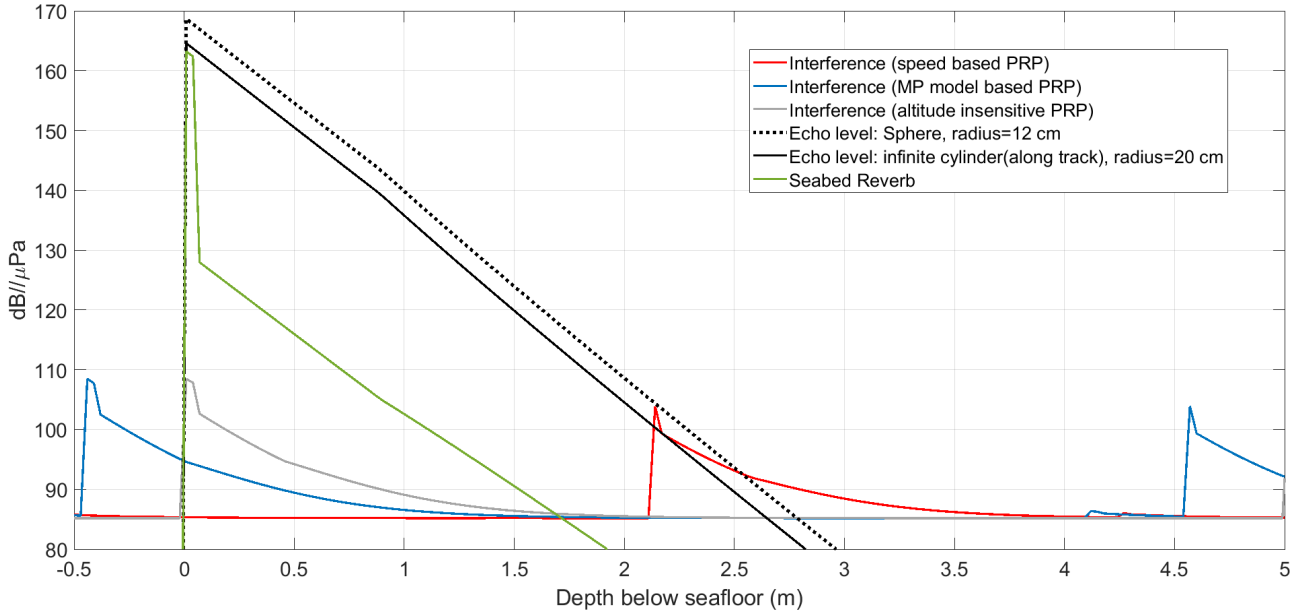

Fig. 3. Downlooking LFSAS performance as a function of depth into the seabed for two targets buried in medium sand, imaged from an altitude of 5 m. Interference is the combined interference from ambient noise, electronic noise, and MP, and is shown for: the standard (speed based) calculation of PRP (9), the MP model derived expression for PRP (10)-(13), and the altitude insensitive MP expression (14).

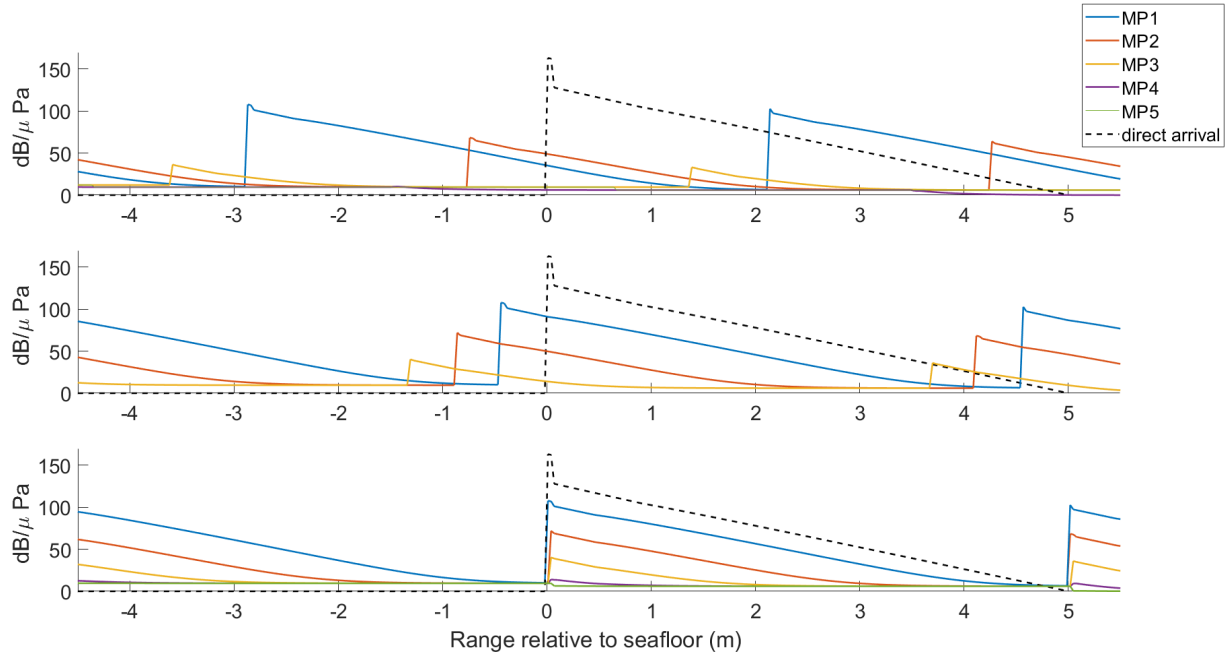

Fig. 4. Acoustic returns from the direct arrival from the ping of interest along with the multipath from 5 pings previous (MP1 being one ping previous and MP5 being 5 pings previous). The top plot is the expected MP return using the speed based PRP (9), the middle plot is for the altitude dependent PRP (10)-(13), and the bottom plot is for altitude independent PRP (14).

multipath for each altitude update. Such altitude sensitivity and model dependence can be avoided if we instead use the following expression for PRP

$$PRP = \left\lfloor \frac{C_w L_a}{4vh} \right\rfloor \frac{2h}{C_w} \tag{14}$$

This expression makes the PRP a multiple of the vehicle altitude such that all the multipath returns stack towards the beginning of the seabed signal (Fig. 4 bottom), rather than shifting the largest multipath contributor from the middle of the signal (Fig. 4 top) to the end (i.e., just outside the

maximum range), as the previous expression did (Fig. 4 middle). Although expression (14) utilizes vehicle altitude, we consider it altitude insensitive since it is not as sensitive to altitude changes as the model based expression for PRP. Expression (14) is only suitable for applications where we are interested in deeply buried targets because we likely won't be able to detect targets at or just below the sediment-water interface (first 5–7 cm), as the total interference (interference plus seabed reverb) will likely be higher than many target responses (Fig. 3 , gray line). For some purposes, this may be considered an appealing trade off, as relative to expression 10, expression 14 makes no assumptions on which MP arrival will interfere with the direct signal and controls all the MP arrivals instead.

One could modify expression (14) such that the multipath appears just after the sediment interface response has dissipated and thus no longer combines with the sediment interface response

$$PRP = \left\lfloor \frac{C_w L_a}{4vh} \right\rfloor \frac{2h}{C_w} - K, \tag{15}$$

where K is a constant delay with units of seconds. By delaying the MP interference to just outside the sediment interface return we mitigate the risk of the sediment interface response and MP combining together to mask target responses. The caveat of such a method is that the sediment interface response duration is variable and difficult to predict (here we are assuming the interface response only lasts one depth resolution cell). This method also risks interfering with the response of any weak targets. In the rest of this paper our performance prediction model will utilize the altitude sensitive expression (10) for the PRP.

IV. Results and Discussion

A. Depth Performance

Here, we will evaluate the maximum target detection depth at nadir (90° grazing angle). For simplicity, all cylinders presented in this section were simulated trending in the along track direction. The maximum buried object detection depth is highly dependent on target shape and size, as well as sediment type (Fig. 5). Due to increased sub-bottom penetration, buried objects can be detected significantly deeper in silt than sand. In sand, the finite and infinite cylinder have nearly identical performance. This is because the performance in the sand sediment is largely limited by attenuation. In silt, small diameter (less than ~ 40 cm) infinite cylinders show significantly deeper maximum detection depth compared to finite cylinders of the same diameter, while at larger diameters the finite and infinite cylinders have identical performance. As described earlier, as the cylinder length becomes large relative to the range to the seabed, it effectively becomes an infinite cylinder.

B. Across track performance envelope

Here, we have used the sonar performance model to demonstrate the expected signal-to-total-interference-ratio (SIR) as a function of across track range and depth below the seabed.

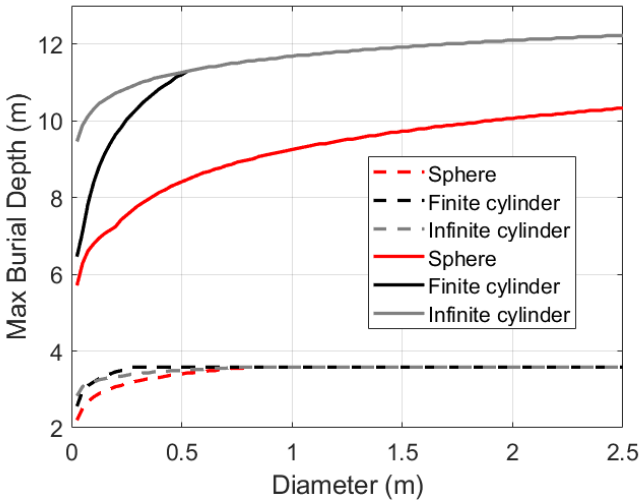

Fig. 5. Deep water maximum target detection depth below seafloor of spherical and cylindrical targets as a function of target size buried in a medium sand (dashed lines) and silt (solid lines).

The across track performance envelopes demonstrate the SIR of a target located at each location in the imaging space (rather than an individual target located at a single location).

Figure 6 illustrates surface and sub-bottom reverberation level for silt. We note a degradation as a function of range and depth into the sediment due to increased transmission and attenuation loss, as well as decreases in the seabed backscattering strength away from nadir (90° grazing angle).

The sphere target strength is independent of target orientation and thus the performance envelope is not heavily dependent on the across track position. For the sphere, the only SIR variation we see is at long range (Fig. 7), due to signal attenuation.

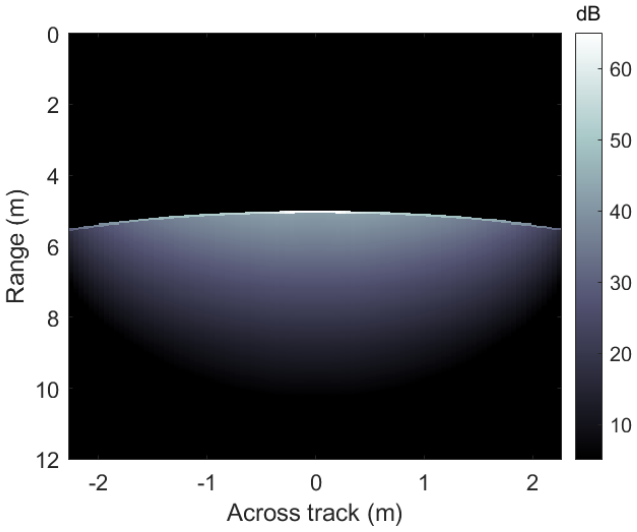

Fig. 6. Across track surface and sub-bottom reverberation level envelope for silt sediment.

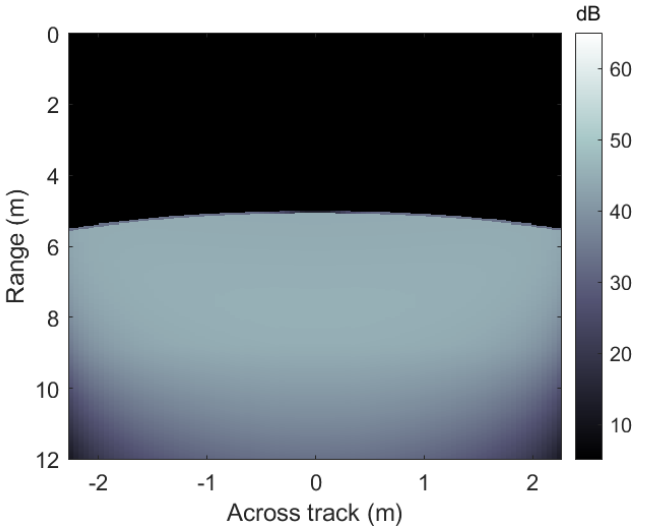

Fig. 7. Across track sonar performance envelope for a 12 cm diameter sphere buried in silt sediment.

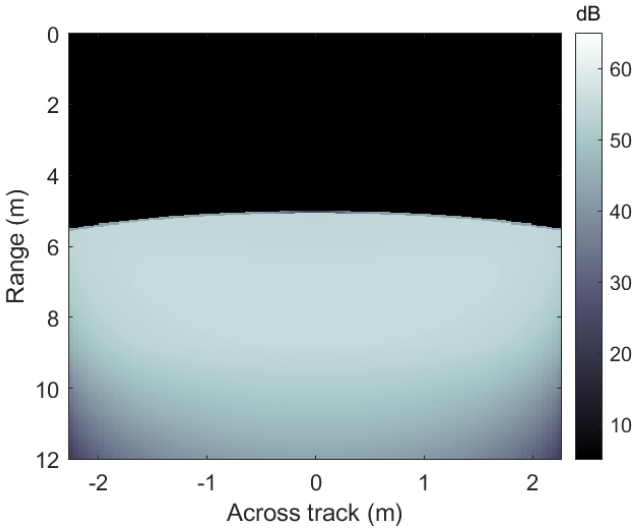

Fig. 8. Across track sonar performance envelope for a 12 cm diameter cylinder trending in the along track direction and buried in a silt sediment.

For cylinders trending in the across track direction we observe a significant difference between finite and infinite cylinders. The infinite cylinder has a similar across track envelope to that seen in Fig. 8, except with a target strength that is about 10 dB higher. The finite cylinder, however, has a significantly different response. For the finite cylinder trending in the across track direction, the performance envelope experiences constructive and deconstructive interference at particular angles, creating a banding effect in the image (Fig. 9). Additionally, outside of the normal to the cylinder axis, the acoustic response is significantly reduced. This highlights the importance of steering the array over a wide range of angles in the across track direction, which ensures we illuminate the target at various aspect angles, thus increasing our chances of target detection [14].

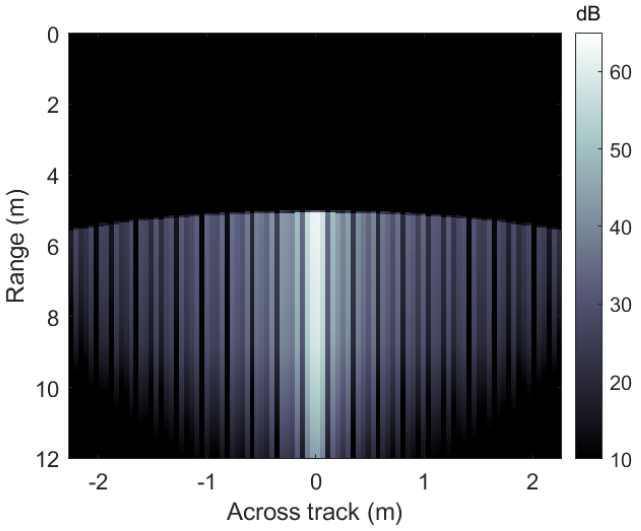

Fig. 9. Across track sonar performance envelope for a 12 cm diameter finite cylinder trending in the across track direction and buried in a silt sediment.

C. Area Coverage Rate

The downlooking LFSAS ACR is dependent on the vehicle velocity and swath width. Using the across track performance envelope, we can estimate the ACR of the downlooking LFSAS as a function of vehicle velocity. We will assume the maximum limit for the ACR will be the –3 dB across track beamwidth of the transmitter. At 5 m altitude, the upper bound on the double-sided across track swath is 4.5 m. Here, we will consider the maximum achievable swath to be the maximum across track distance where we can detect targets (with 10 dB SNR) to at least 1 m below the seabed interface.

For sub-bottom imaging purposes, the maximum swath, and thus full ACR, can be achieved in all sediment types simulated, giving an ACR of 0.017–0.048 km^2/h, depending on vehicle speed.

For target detection, the achievable ACR is dependent on the target characteristics (shape, size, and orientation), but is generally limited by the critical angle and attenuation coefficient of the sediment type the target is buried in. In silt sediment, the critical angle is zero degrees and the signal attenuation is low. Thus, all targets can be detected across the entire swath. In medium sand the ACR is highly dependent on the target size. For small diameter (less than 40 cm) spheres and cylinders trending in the along track direction, the ACR in medium sand is significantly constrained, as their target strengths are not high enough to allow for detection. Small spheres and small cylinders trending in the along track direction can be detected to a double sided swath of 2.8 m in medium sand, giving an ACR range of 0.011–0.031 km^2/h (Figure 10). For finite cylinders trending in the across track direction, the maximum swath is limited by the across track target strength response. For the case of medium sand, this equates to a swath width of 2.3 m and an expected ACR of

0.008–0.025 km^2/h (Figure 10).

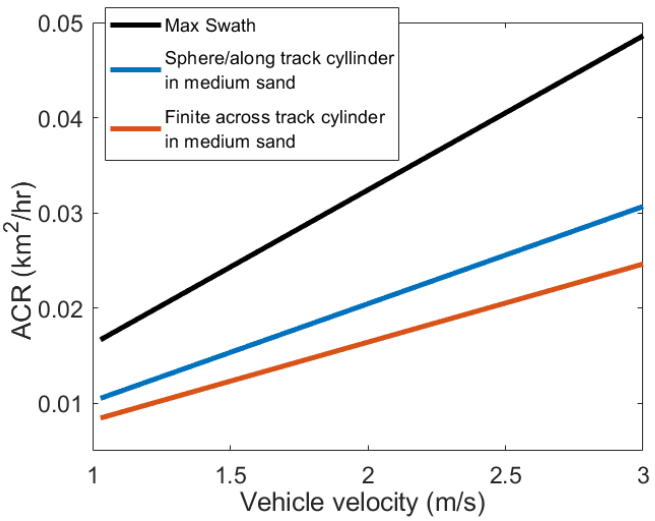

Fig. 10. Area coverage rate as a function of vehicle velocity for small targets imaged at an altitude of 5 m.

Large targets (diameters greater than 40 cm) have target strengths sufficient for detection, even in the presence of strong signal attenuation in the sediment. Thus, in most cases the maximum swath can be achieved. Since larger targets can still be effectively imaged at lower resolutions, it is possible to further increase the ACR by operating at a higher altitude.

V. Conclusions

In this paper, we introduced a new sonar performance prediction model for downlooking LFSAS. We demonstrated methods to mitigate MP interference through a judicious choice of pulse repetition period. By altering the period, we can avoid MP interference and extend the buried target detection depth to the ambient/electrical noise limit. Without MP interference, buried target detection becomes dependent on the environment, target size and orientation. While operating at 5 m altitude, LFSAS can detect targets to burial depths of up to 3.5 m in sand and 6–12 m in silt. The across track performance envelope and ACR are highly dependent on target size. Large (greater than 40 cm diameter) targets can achieve full ACR, whereas the detection swath for small targets is limited by the sediment attenuation and target response.

Appendix A
Multipath Modeling

In this paper, the primary source of MP interference is assumed to be the sound traveling between the vehicle and the seabed multiple times. For modeling purposes, we treat the vehicle as a perfect mirror that reflects all the sound incident upon it. The MP history from M previous pings must be tracked in order to effectively account for all the MP interference contributions from the sonar to seabed to sonar path (and subsequent multiples after that). Here, we keep track of the MP history of five previous pings from the current one to ensure we capture all possible sources of MP that may overlap with the time interval of the current ping of interest. Each ping will have several MP bounces before dissipating to an amplitude below the ambient noise. We set an upper bound on the number of MP bounces to model for each ping (N) using

$$N = \left\lceil \frac{C_w PRP}{2h} \right\rceil + 3 \tag{16}$$

The first term in the equation represents the maximum number of times the multipath can travel between the vehicle and the seabed interface before the next ping starts. The addition of three is used to ensure that we don't miss any MP that may still be propagating during the start of the next ping.

To determine how long a given previous ping contributes to the interference we must account for the vehicle size and receiver beamwidth in both the along track and across track direction. In the along track direction, we calculate the maximum angular extent (ϕ_x) in both the fore and aft direction (relative to the vehicle heading), using (17) and (18), respectively.

$$\phi_{xf} = \begin{cases} \tan^{-1}\frac{L_a}{2R}, & \text{if } R_x > \frac{L_a}{2} \\ \frac{\theta_x}{2}, & \text{otherwise} \end{cases} \tag{17}$$

$$\phi_{xa} = \begin{cases} \tan^{-1}\frac{L_v - L_a}{R}, & \text{if } R_x > L_v - \frac{L_a}{2} \\ \frac{\theta_x}{2}, & \text{otherwise} \end{cases} \tag{18}$$

Here, L_v is the length of the vehicle in the along track direction, L_a is the length of the receiver array, $R_x = R\tan\frac{\theta_x}{2}$, and R is the path length of a given multipath return m

$$R = r + (1 + 2m)h \tag{19}$$

where h is the vehicle altitude above the seabed and r is the path length along the transmitter line of sight. In the across track direction, this maximum angular extent (ϕ_y) can be calculated using a single equation

$$\phi_y = \begin{cases} \tan^{-1}\frac{W_v}{R}, & \text{if } R_y > W_v \\ \frac{\theta_y}{2}, & \text{otherwise} \end{cases} \tag{20}$$

where, W_v is the half width of the vehicle in the across track direction and $R_y = R\tan\frac{\theta_y}{2}$.

Based on the sonar equation, the strength of each ping's MP return ($\hat{a}(n,r)$) as a function of range (r) can be modeled as

$$\hat{a}(n,r) = SPL(n) - TL(n,r) + SS(n,r) + DI(r) \tag{21}$$

where $SPL(n)$ is the sound pressure level that arrives at the vehicle just before the next bottom multiple. This representation ensures that we are only including the sound intensity that actually reaches the vehicle in our calculations. Accurately determining this value is non-trivial. We estimate it based on the backscattering coefficient at normal incidence. The $SS(n,r)$ term is the sediment scattering response

$$SS(n,r) = \begin{cases} 10\log_{10}\sigma_s A(n,r), \ , & \text{if } r < R + \delta z \\ 10\log_{10}\sigma_v V(n,r), & \text{otherwise} \end{cases} \tag{22}$$

where σ_s and σ_v are the backscattering cross sections at the sediment interface and volume, respectively, and $A(n,r)$ and $V(n,r)$ represent the ensonified area and volume, respectively. The total MP interference from each ping ($\hat{A}$) is then accumulated into a full MP history as

$$\hat{A} = \sum_{m=1}^{M} \sum_{n=1}^{N} \hat{a}(n,r). \tag{23}$$

REFERENCES

[1] S.-M. Steele, R. Charron, J. Dillon, and D. Shea, "Performance prediction for a low frequency ultra-wideband synthetic aperture sonar," *Proc. IEEE/MTS OCEANS, Seattle, WA, USA*, 2019.

[2] D. R. Jackson and M. D. Richardson, *High-Frequency Seafloor Acoustics*. Springer, 2011.

[3] J. Dillon and R. Charron, "Resolution measurement for synthetic aperture sonar," *Proc. IEEE/MTS OCEANS, Seattle, WA, USA*, 2019.

[4] J. Dillon, S.-M. Steele, R. Charron, D. Shea, N. Smith, J. Albiez, and A. Duda, "Synthetic aperture sonar nadir gap coverage with centimetric resolution," *Global Oceans 2020: Singapore – U.S. Gulf Coast*, 2020.

[5] U. of Washington, *APL-UW High-Frequency Ocean Environmental Acoustic Models Handbook*, 1994.

[6] A. Maguer, E. Bovio, W. L. J. Fox, and H. Schmidt, "In situ estimation of sediment sound speed and critical angle," *The Journal of the Acoustical Society of America*, vol. 108, no. 3, p. 987, Oct 2000.

[7] E. I. Thorsos, D. R. Jackson, and K. L. Williams, "Modeling of subcritical penetration into sediments due to interface roughness," *The Journal of the Acoustical Society of America*, vol. 107, no. 1, pp. 263–277, Feb 2000.

[8] D. Jackson, K. Williams, E. Thorsos, and S. Kargl, "High-frequency subcritical acoustic penetration into a sandy sediment," *IEEE Journal of Oceanic Engineering*, vol. 27, no. 3, pp. 346–361, Jul 2002.

[9] J. E. Moe and D. R. Jackson, "Near-field scattering through and from a two-dimensional fluid–fluid rough interface," *The Journal of the Acoustical Society of America*, vol. 103, no. 1, pp. 275–287, Jan 1998.

[10] G. M. Wenz, "Acoustic ambient noise in the ocean: Spectra and sources," *The Journal of the Acoustical Society of America*, vol. 34, no. 12, pp. 1936–1956, 1962.

[11] D. Tamsett, "Geometrical spreading correction in sidescan sonar seabed imaging," *Journal of Marine Science and Engineering*, vol. 5, no. 4, p. 54, 2017.

[12] R. J. Urick, *Principles of Uncerwater Sound*. Peninsula Publishing, 2013.

[13] L. J. Cutrona, "Additional characteristics of synthetic-aperture sonar systems and a further comparison with nonsynthetic-aperture sonar systems," *The Journal of the Acoustical Society of America*, vol. 61, no. 5, p. 1213–1217, 1977.

[14] S. Schock, J. Wulf, G. Quentin, and J. Sara, "Synthetic aperture processing of buried object scanning sonar data," *Proceedings of OCEANS 2005 MTS/IEEE*, vol. 26, no. 4, Oct 2001.